



Quantifying CMIP6 model uncertainties in extreme precipitation projections

Amal John, Hervé Douville, Aurélien Ribes, Pascal Yiou

► To cite this version:

Amal John, Hervé Douville, Aurélien Ribes, Pascal Yiou. Quantifying CMIP6 model uncertainties in extreme precipitation projections. 2021. hal-03464913v1

HAL Id: hal-03464913

<https://hal.science/hal-03464913v1>

Preprint submitted on 3 Dec 2021 (v1), last revised 22 Mar 2022 (v2)

HAL is a multi-disciplinary open access archive for the deposit and dissemination of scientific research documents, whether they are published or not. The documents may come from teaching and research institutions in France or abroad, or from public or private research centers.

L'archive ouverte pluridisciplinaire **HAL**, est destinée au dépôt et à la diffusion de documents scientifiques de niveau recherche, publiés ou non, émanant des établissements d'enseignement et de recherche français ou étrangers, des laboratoires publics ou privés.

Quantifying CMIP6 model uncertainties in extreme precipitation projections.

Amal John ^{*a c}, Hervé Douville^a, Aurélien Ribes^a and Pascal Yiou^b

^aCentre National de Recherches Météorologiques, Météo-France, CNRS, Toulouse,
France

^bLaboratoire des Sciences du Climat et de l'Environnement, UMR 8212
CEA-CNRS-UVSQ, IPSL & U Paris-Saclay, 91191 Gif-sur-Yvette, France

^cUniversité de Toulouse, France

October 2021

*Corresponding Author

DESR/CNRM/GMGEC/CLIMSTAT

CNRM/Météo-France

42, avenue Gaspard Coriolis

Toulouse, 31100, France

john.amal@meteo.fr

Abstract

Projected changes in precipitation extremes and their uncertainties are evaluated using an ensemble of global climate models from phase 6 of the Coupled Model Intercomparison Project (CMIP). They are scaled by corresponding changes either in global mean surface temperature (ΔGSAT) or in local surface temperature (ΔT) and are expressed in terms of 20-yr return values (RV20) of annual maximum one-day precipitation. Our main objective is to quantify the model response uncertainty and to highlight the regions where changes may not be consistent with the widely used assumption of a Clausius-Clapeyron (CC) rate of $\approx 7\%/K$. When using a single realization for each model, as in the latest report from the Intergovernmental Panel on Climate Change (IPCC), the assessed inter-model spread includes both model uncertainty and internal variability, which can be however assessed separately using a large ensemble. Despite the overestimated inter-model spread, our results show a robust enhancement of extreme precipitation with more than 90% of models simulating an increase of RV20. Moreover this increase is consistent with the CC rate of $\approx 7\%/K$ over about 94% of the global land domain when scaled by (ΔGSAT). Our results also advocate for producing single model initial condition ensembles in the next CMIP projections, to better filter internal variability out in estimating the response of extreme events.

Keywords Climate change, Precipitation, Uncertainty, Extremes

1 Introduction

Global climate models provide an increasingly comprehensive representation of the climate system and are used as a primary tool for understanding and projecting changes in climate mean, variability and extremes due to human activities. The Intergovernmental Panel on Climate Change (IPCC) in its sixth assessment report (AR6) has re-estimated an increase in global mean surface temperature of 1.0°C since the industrial revolution. This anthropogenic global warming is reckoned to have long-term consequences on all components of the climate systems, including changes in the precipitation distribution. Several generations of multi-model simulations based on the Coupled Model Intercomparison Project (CMIP), supported by observational evidence, show that both the frequency and intensity of extreme precipitation events have increased with the global increase in the

38 temperature recorded over recent decades (Allen and Ingram, 2002; Asadieh and Krakauer, 2015;
39 Scherrer et al., 2016; Karl and Easterling, 1999; Kharin et al., 2013; Min et al., 2011; O’Gorman,
40 2015). This is also documented in the IPCC special report on Managing the Risks of Extremes
41 Events to Advance Climate Change Adaptation (SREX, Seneviratne (2012)).

42 In the absence of moisture limitation and of significant dynamical response, the extreme
43 precipitation intensity is expected to increase exponentially with the atmospheric temperature at
44 a rate determined by the Clausius–Clapeyron (CC) relationship. A robust scaling of precipitation
45 extremes with global warming across scenarios was confirmed by Li et al. (2020) who found that
46 changes in precipitation extremes follow changes in global warming at roughly the CC rate of \approx
47 $7\%/^{\circ}\text{C}$ in the latest-generation CMIP6 models. Several studies based on climate model simulations
48 show a future increase of precipitation extremes with the temperature at a rate comparable to or
49 higher than the CC rate (Li et al., 2020; Kharin et al., 2007; Pall et al., 2007; Allan and Soden,
50 2008; Sugiyama et al., 2010; Kao and Ganguly, 2011; Muller et al., 2011). However, wet extremes
51 are not expected to intensify in all regions (Trenberth, 2011; Pfahl et al., 2017).

52 All these studies either show the multi-model mean or median and have not yet assessed the
53 uncertainties in global CMIP6 projections. A suite of different model projections often exhibits a
54 large spread (Lehner et al., 2020) and can even disagree on a particular region becoming wetter
55 or drier (sign change in the future). Even where there is an overall consensus among the models
56 on the sign of changes in the projected extremes due to a warmer climate, the magnitude of such
57 changes can differ considerably. Though the climate models have improved over recent decades
58 (Wyser et al., 2020; Zelinka et al., 2020), these improvements do not result in a reduced spread
59 among the projections. Thus, the main focus of this paper is to quantify the model uncertainties
60 in extreme precipitation projections based on CMIP6 models. We also aim to provide a blueprint
61 on using these projections to identify regions that are consistent with the CC rate and those that
62 are not.

63 The changes in extreme precipitation against a backdrop of warming climate arise both due
64 to thermodynamic and dynamic effects (Pfahl et al., 2017). A sub-CC relation or even negative de-

pendence on global mean temperature has been found for precipitation extremes over some regions, especially over the climatologically dry oceanic regions in the subtropics, presumably as a result of decreasing moisture availability and enhanced large-scale subsidence (Berg et al., 2009; Hardwick Jones et al., 2010; Utsumi et al., 2011; Pfahl et al., 2017). But the question of an appropriate choice of temperature for scaling extreme precipitation is still an open question and the available studies differ in scope (Zhang et al., 2019; Schroer and Kirchengast, 2018; Sun et al., 2021). There is a large-scale discrepancy in the warming over the continental landmass and oceans with certain regions over the ocean experiencing a negligible change in the projected surface temperatures. The larger warming observed over land than over the ocean may result in a lower scaling with local mean temperature, which may not be considered as a sub-CC scaling rate (Wang et al., 2017). Any departure from the CC rate can be an indication of a dynamical response which may be either amplified or offset by a thermodynamic response regionally (Pfahl et al., 2017; Sherwood et al., 2010; O’Gorman, 2015). Thus here we explore changes in extreme precipitation simply scaled by either global mean or local surface air temperature changes.

Several studies (Alexander et al., 2006; Tebaldi et al., 2006; Sillmann et al., 2013a,b) have used various indices as a proxy for different features of precipitation extremes. Here we focus on extreme events with typical return periods of 20 years (or 20-year return values, RV20) as estimated from the annual maximum one-day precipitation (RX1DAY). Projected long-period RX1DAY return value changes are larger than changes in mean RX1DAY and increase with increasing rarity (Mizuta and Endo, 2020; Wehner, 2020).

The goal of this study is to assess the uncertainties of projected changes in extreme precipitation based on the multi-model CMIP6 ensemble, to discuss the limitations of assessing the inter-model spread using such ensembles of opportunity, and to highlight the regions where projected changes may not be consistent with the widely used assumption of a Clausius-Clapeyron rate of $\approx 7\%/K$ (Kharin et al., 2013; Westra et al., 2013; Seneviratne et al., 2021). For this purpose, we use 34 CMIP6 models and focus on a single greenhouse gas concentration scenario. The total spread in this ensemble is therefore a combination of both model response uncertainty and internal variability. Therefore, we also assess the contribution of internal variability by analyzing the pro-

jected changes of the RV20 in the CanESM5 model with 25 realizations of the same concentration scenario.

The rest of the paper is structured as follows. We start by introducing in section 2 the models and methods used in this study. Turning to the results in section 3, we address the uncertainties in the model projections along with discussions on the role of internal variability using 25 ensemble member simulations from the CanESM5 model. Also, discussing the role of local and global temperature in scaling. Section 4 summarises the major findings. Other supporting figures and tables are available in the online supplementary material.

2 Data and methods

2.1 Data

Daily precipitation data from 34 global climate models from the CMIP6 repositories (Eyring et al., 2016) are used in this study. We combine the historical simulations (1850-2014) with one shared socioeconomic pathways (SSPs) projections (O’Neill et al., 2016) running from 2015 to 2100. The ”end of the road” scenario SSP5-8.5 with the highest emissions is used to get maximum climate change signals and, therefore, better isolate the forced RX1DAY response from internal variability without using large initial condition ensembles (which are only available for a limited number of models). We use the one-model-one-vote approach i.e., without giving any particular weights, although there are dependencies across models (eg Knutti and Masson (2013); Bador et al. (2018)). For each CMIP model involved, only one member of the historical and SSP5-8.5 simulations are used — a treatment that is consistent with the recent IPCC AR6, and which ensures that all models are treated equally. As the total uncertainty in the projected changes is the sum of both model uncertainties and internal climate variability, we here also analyze a single model initial condition large ensemble, provided by the CanESM5 model (Swart et al., 2019), with 25 individual members. Hence we can quantify an upper bound for the total uncertainties.

2.2 Climate extreme indices and GEV analysis

We first interpolate the daily precipitation data for each model into a $1^\circ \times 1^\circ$ grid using a first-order conservative remapping. This helps us to compare the multiple models with different

resolutions by reducing the differences in the spatial scales from CMIP6 models (1-2°). For each model at each grid point and each year, we calculate the annual maximum daily precipitation (RX1DAY), which is an extreme index defined by the expert group on Climate Change Detection and Indices (ETCCDI) (Karl et al., 1999; Peterson et al., 2001).

We then analyze the return values of RX1DAY, in line with some previous studies of Kharin et al. (2013) and Wehner et al. (2020). Following their approach, we modeled the annual maxima of precipitation at each grid point using a Generalized Extreme Value Distribution (GEV) in order to estimate large return values with return periods of 20 years. The GEV estimation is implemented for two time windows, which are, 1951–2014 for the historical period and 2051–2100 for the late 21st century.

The cumulative distribution function for a GEV distribution for a random variable X is:

$$F(x) = \begin{cases} \exp \left[- \left(1 + \xi \frac{x-\mu}{\sigma} \right)^{-\frac{1}{\xi}} \right], & \xi \neq 0 \\ \exp \left[- \exp \left(-\frac{x-\mu}{\sigma} \right) \right], & \xi = 0 \end{cases} \quad (1)$$

where μ , $\sigma > 0$, and ξ are the location, scale, and shape parameters, respectively. Having fitted GEV distribution, the precipitation extremes of our interest are defined as the 20-year return values. Return values are calculated as the exceedance of the annual extreme with probability p or as the quantile functions of a GEV distribution. The changes in the intensities of extremes events can accordingly estimate for different future periods or warming levels. Changes in the future (2051–2100) are computed with respect to the historical period (1951–2014), while changes at different warming levels are expressed relative to their intensity during the preindustrial period (1850–1900).

2.3 Global warming Levels

We frame the projections by considering the changes at a specified global warming target of 1.5, 2, and 3 K above the pre-industrial levels. Climate sensitivity, or the simulated global mean surface air temperature response to more comprehensive radiative forcings, is different across different models (Vial et al., 2013; Lee et al., 2021). As a consequence, the point in time when

specified global warming levels (GWLs) are achieved by each model differs largely. Models with higher climate sensitivity reach specified GWLs earlier than others. However, some models may not even reach the highest specified GWL before 2100. The first year when GWLs are reached for the 34 CMIP6 models used in this study under the scenario SSP5-8.5 is shown in the supplementary material (Table S. 1). The extreme precipitation statistics are then calculated for each model individually over 21 years, extending from 10 years before and after the "central year".

2.4 Scaling of extreme precipitation with local and global temperature changes.

We scale changes in extreme precipitation ($\Delta RV20$) with both global mean surface air temperature change ($\Delta GSAT$) and local surface air temperature change (ΔT). $\Delta GSAT$ is calculated as the difference between the areal mean surface temperatures for the projected period and reference period (cf. Table S1). Similarly, ΔT is estimated as the local change in the climatological surface temperature or the rate of change of mean surface temperature at each grid point for the same periods as above. Instead of considering the linear rate of change ($R_{lin} = \Delta P_{ext} / \Delta t_{surf}$) of the extreme precipitation, we assume a multiplicative rate of change, i.e., $\Delta P_{ext} = (1 + R_{mul})^{\Delta t_{surf}}$. The multiplicative rate of change is thus calculated as

$$R_{mul} = (1 + \Delta P_{ext})^{\frac{1}{\Delta t_{surf}}} - 1, \quad (2)$$

where ΔP_{ext} is the change in precipitation extremes (here, $\Delta RV20$) and Δt_{surf} is the change in the surface temperature (either $\Delta GSAT$ or ΔT). Both the linear and the multiplicative rates become approximately equal ($R_{lin} \approx R_{mul}$) when $\Delta RX1DAY \ll 1$. Another important point to note here is that for scaling with local temperature changes we masked the regions where the temperature changes are too small (i.e, $\Delta T \ll 1$) to avoid the infinite scaling while using equation 2. The masking is done only for those models which show $\Delta T \ll 1$, while we keep the others so that the results are calculated for the models which project a minimum surface warming.

2.5 Hypothesis Testing.

We also aim to identify the regions where the change in extreme precipitation may occur at a super-CC rate or sub-CC rate. In the latest IPCC report, (Seneviratne et al., 2021) conclude with

high confidence that precipitation extremes are controlled by both thermodynamic and dynamic processes, and that warming-induced thermodynamic change results in an increase in extreme precipitation at a rate that closely follows the CC relationship at the global scale. Any departure from the CC rate could therefore indicate an additional large-scale dynamical response (Pfahl et al., 2017). Note however that our analysis is only based on global climate models with parameterized convection so that the dynamical response here does not account for explicit mesoscale changes in the storm dynamics that could also modulate the extreme precipitation response (e.g., Chan et al. (2020)).

The blueprint we provide for this in section 4 will be a stepping zone to an extended analysis on this matter. This can provide us with much confidence in the areas that are dominated by warming and those regions the circulation patterns matter. For this, we use a simple hypothesis testing, where we identify the region where, e.g., there is no change, using the 80% confidence intervals we obtained from the multi-model framework. Anytime, where the targeted R_{mul} (rate of change of RV20 with temperature) does not fall within the confidence interval calculated from the 34 models, we conclude that our hypothesis is rejected. When it comes in the range of the confidence interval, we accept the null hypothesis, and the regions are identified accordingly. To identify the regions with no change, we consider the null-hypothesis $R_{mul} = 0\%/C$, while $R_{mul} = 7\%/K$ is used as our second hypothesis to find regions of sub-, super-, or consistent with the CC rate.

3 Results

3.1 Intensification of extreme precipitation

Figure 1 shows the analysis for the median, 10th, and 90th percentiles along with the uncertainty range, which is, the difference between the 90th and 10th percentiles, of the extreme precipitation changes scaled by both the global mean ($\Delta GSAT$, left panel) and local mean (ΔT , right panel) surface air temperature changes. The extreme precipitation rate as a function of both $\Delta GSAT$ and ΔT shows a clear increase in its intensity with respect to the historical period (1951-2014). The global average of the multi-model median changes is 5.897%/K (Figure 1 c) for the

195 scaling with ΔGSAT while for that of ΔT it is 6.332%/K (Figure 1 d). These values are slightly
196 short of the CC rate of 7%/K and the global average values do not appear to vary strongly with
197 our choice of scaling temperature.

198 From the maps, figure 1 c, d the overall large-scale patterns of change remain similar for
199 both temperature scalings, although changes are a bit more pronounced for the scaling with local
200 temperatures. The largest percentage of increase occurs over the tropical areas followed by the
201 high latitudes for the global temperature scaling. For the local scaling, the largest percentage of
202 changes occurs over the tropics followed by the mid-latitude oceans. The disproportionate warming
203 over the continental landmass and oceans can be a major reason for these differences (Wang et al.,
204 2017). Certain regions over the ocean like the north Atlantic and the southern oceans in figure 1c
205 are characterized by moderate to high scaled changes in precipitation extremes, which can be linked
206 to the negligible changes in the projected local surface temperatures.

207 Changes in extreme precipitation with ΔGSAT as well as ΔT vary substantially across the
208 globe. Over most of the mid-latitude land areas, changes do not strongly depend on the scaling
209 method and exhibit a sub-CC rate of 0-4%/K. Over the subtropics, the assessed rate of change
210 deviates further from the CC rate. In particular, there are high rates (super CC) over the Sahara
211 and the intertropical convergence zone (ITCZ), while the climatological dry areas like the basins
212 of the South Pacific, the north and the south Atlantic, and the south Indian Ocean are marked by
213 reduced, or even negative, rates of change in the extremes. This deviation from the global averaged
214 CC rate ($\approx 7\%/K$) indicates some other factors apart from the thermodynamic features might be
215 at play. Notably, a remarkable property is the increased multi-model spread over these regions
216 (ref., supplementary material), in line with the less robust dynamical response across global climate
217 models (Pfahl et al., 2017). Large departures, whether it is positive or negative, from the CC rate
218 are associated with a larger inter-model spread, suggesting that these regions may be influenced
219 by less robust changes in atmospheric circulation, possibly related to model-dependent patterns
220 of sea surface temperature anomalies or land-sea temperature contrasts (Douville and John, 2021).
221 Another noticeable feature is the impact of the scaling temperature over the northern high-latitudes.
222 This is partly linked to the Arctic amplification, where the Arctic region gets warm more than twice

223 as fast as the global average (Cohen et al., 2014).

224 **3.2 Range of Projected responses in extreme precipitation**

225 The figure 1. a, b, e and f illustrate the 10th and 90th percentiles of extreme precipitation
226 rates for both global and local warming. The lower and the upper tails of distribution help us
227 to study the worst possible case scenarios and more importantly quantify the uncertainties. The
228 lower tails of extreme precipitation rates are characterized by large-scale features like the negative
229 scaling over the subtropical oceans in the western continental boundaries for both global and local
230 temperature scaling. It is important to note that these regions are predominantly dry areas due
231 to the descending branches of the Hadley Cell. The rest of the globe is marked by very small
232 changes either positive or negative that are very close to zero. However, the 90th percentile maps
233 or the upper tail of the distribution show a strong positive increase in precipitation extremes almost
234 everywhere around the globe. These are consistent with super-CC rates (stippling) for the scaling
235 with global warming and, to a large extent, with local warming. Typical to the local warming
236 scaling, the northern mid and high latitudes land areas are not stippled. This means the rate of
237 changes in extreme precipitation with local warming is sub-CC over these regions even for the 90%
238 quantiles. Moreover, this is coherent and non-conflicting for all the three maps in the right panel
239 of figure 1 b, d, f. This results directly from a larger and consistent local warming over these areas,
240 especially in the Arctic.

241 Another noticeable result is the zero or low-density stippling over the tropical Atlantic ocean,
242 Southern Europe, Chilean Coast, and South Africa in all maps of both global and local temperature
243 scalings (figure 1). This implies a consistent sub-CC rate over these areas irrespective of the scaling
244 choice. We speculate the circulation changes, such as a broadening of the subtropical subsidence
245 region might be responsible for this (Pfahl et al., 2017). Indeed this kind of extension can effectively
246 replace a low-level moisture convergence zone with a regime with low-level divergence where there
247 is a weaker connection between the projected changes in precipitable water versus temperature.

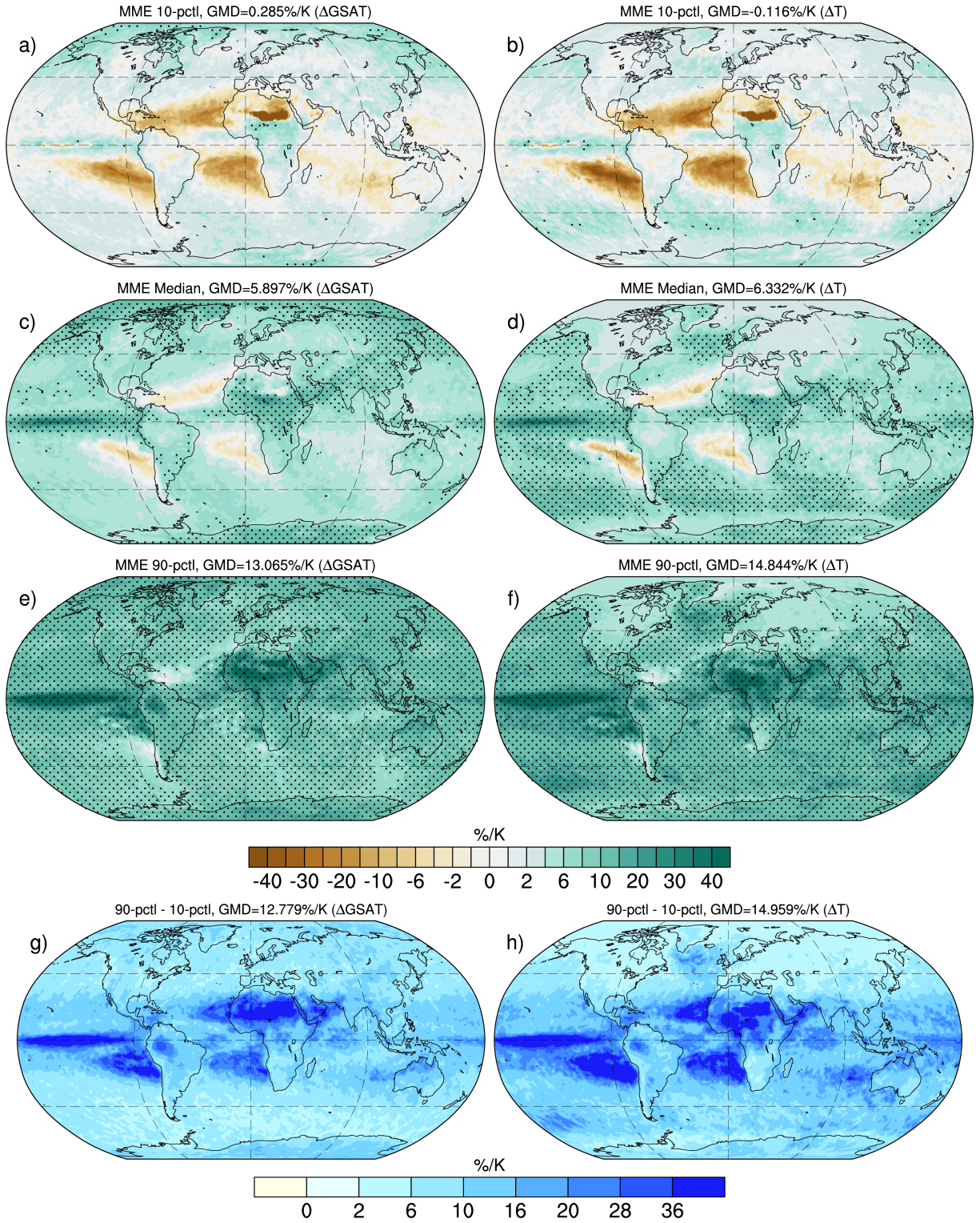


Figure 1: Projected relative changes (%/K) in 20-yr return values of RX1DAY scaled by both global mean surface temperature change (ΔGSAT in K, left panel) and local mean surface temperature change (ΔT in K, right panel). The changes are calculated for the future period of 2051-2100 relative to the historical period of 1951-2014 using the SSP5-8.8 scenario. (a),(b) show the 10% quantile maps, (c),(d) show the median maps and (e),(f) show the 90% quantile maps, calculate from the CMIP6 multimodel ensemble. The bottom panel shows the width of the confidence range of extreme precipitation, computed as the difference between the 90% and 10% quantile maps. Stippling highlights the grid cells where the rate of change is more than 7%/K. GMD denotes the global mean differences.

248 The bottom panels (g, h) in figure 1 shows the difference between the 10th and 90th percentile
 249 values as simulated by a single realization from 34 CMIP6 models. The large difference between the
 250 upper and lower quantiles indicates a large spread in extreme precipitation changes. These maps
 251 quantify the uncertainties in extreme precipitation response and the pattern is very similar to those
 252 of the inter-model standard deviation maps as stated earlier in section 3.1 (also ref., supplementary
 253 material). As clearly depicted in these figures, the spread is larger over tropical areas than the
 254 rest of the globe. Particularly, over the tropics, the values are notably large in the regions which
 255 are climatologically dry or wet, e.g., the subsidence zones of the Hadley cells, the ITCZ, and the
 256 Saharan desert. We also see that the overall pattern of the inter-model spread is similar for both
 257 temperature scalings. Table 1 reflects the range of model uncertainty in projecting the changes
 258 in extreme precipitation with respect to both local as well as global warming. It summarizes the
 259 areal averages of the median, 10%-, 90%- quantiles and their difference for the total (global) area,
 260 the global land, and global ocean areas separately. It is clear from the table that the width of
 261 confidence range averaged globally is typically quite large about 14.959% which is slightly more
 262 than two times the CC rate. Several sources of uncertainty can contribute to this spread. We
 263 hypothesize that the extreme precipitation changes are more likely due to different representations of
 264 the relevant physical processes in different models and biases arising from this can lead to projection
 265 uncertainty in general. Moreover, the non-homogeneous temperature gradient from the equator to
 266 the poles and the land/sea temperature differences is also a source of larger uncertainty in the local
 267 temperature scaling maps. Another major and non-negligible source of uncertainty is the internal
 268 climate variability which also gets translated differently into the total uncertainty with the use of
 269 different temperatures for scaling. We discuss the role of internal variability in the next section.

			10	med	90	width (90-10)
Total	GSAT	CMIP6	0.285	5.897	13.065	12.779
		CanESM5	2.077	5.623	9.414	7.337
	T	CMIP6	-0.116	6.332	14.844	14.959
		CanESM5	1.706	6.006	10.772	9.066
Land	GSAT	CMIP6	0.769	6.829	14.760	13.991
		CanESM5	3.137	6.919	10.936	7.799
	T	CMIP6	0.329	5.458	12.602	12.602
		CanESM5	2.358	5.437	8.699	6.341
Ocean	GSAT	CMIP6	0.065	5.472	12.291	12.226
		CanESM5	1.591	5.032	8.721	7.130
	T	CMIP6	-0.317	6.733	15.869	16.186
		CanESM5	1.407	6.266	11.721	10.314

Table 1: Areal mean values (in %/K) of 10%-, 90%- quantiles and median of the extreme precipitation changes scaled by both $\Delta GSAT$ and ΔT over the total global area, global land, and global oceans. The table includes the respective values for both the CMIP6 multi-model changes and CanESM5 multi-ensemble changes.

3.3 Role of Internal Variability

The spread among the single realizations of CMIP6 projections has been interpreted so far as model uncertainty but can also arise from internal variability given the limited sampling. In the case of extreme precipitation changes at a multi-decadal time scale, internal variability was shown to be a major driver due to cancellation between different external forcings (Nath et al., 2018). To get more insight into this, we analyzed the rate of change in precipitation extremes in the 25-member ensemble of the CanESM5 model, and assess the spread across members (figure 2). We consider the large ensemble from CanESM5 as a representative estimate of the internal variability range. It should be however noted that CanESM5 is one of the CMIP6 models showing the highest climate sensitivity. While climate sensitivity does not strongly influence the global mean precipitation response (Pendergrass, 2020), the projected extreme precipitation response may be larger given their strong thermodynamic response. However, this effect is accounted for by the scaling and the globally averaged median values are very close for the CMIP6 ensemble and the CanESM5 ensemble for both scaling with ΔGSAT and ΔT (Table 1). Figure 2 shows the same variables as in figure 1, but we see an obvious visible difference between them along with a few matching large scale patterns. For instance, the rates of change for both ΔGSAT and ΔT match over the climatologically dry regions like the north and south tropical Atlantic oceans as well as over primarily wet regions like the inter-tropical convergence zone. Furthermore, the regions like North American inland, Europe and Eurasia, Chilean Coasts, and South Africa are marked by a sub-CC rate of change with both temperature scales, likewise in figure 1. Another noticeable result here is the changes in the areas that are stippled. CanESM5 shows areas of super-CC ($>7\%/K$) even for the 10th percentile maps which are not observed in the CMIP6 ensemble. While for 90th percentile maps we see a decrease in the regions that are super-CC rated. The range of uncertainties ($7.337\%/K$ for ΔGSAT and $9.066\%/K$ for ΔT) across the CanESM5 ensemble members is evidently less than that across the CMIP6 models. The total uncertainties depicted in Figure 2 (bottom panel) is just the result of internal variability. Table 1 again summarizes the mean value of median, 10%-, 90%- quantiles and their difference for the total (global) area, the global land, and global ocean areas separately.

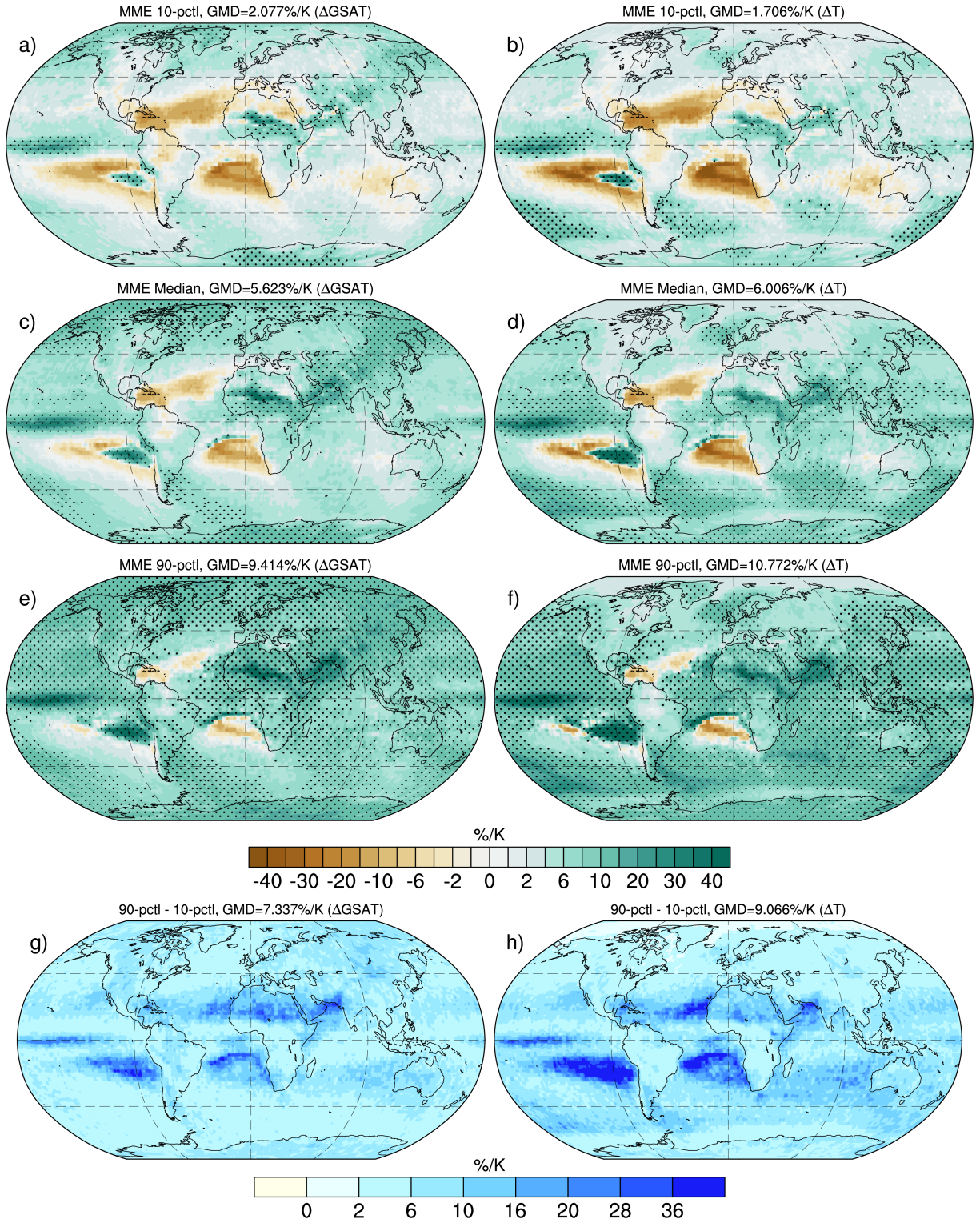


Figure 2: Same as figure 1, but for the ensemble of 25 individual members of CanESM5 model.

298 The similarity between the range of uncertainty for the CMIP6 multi-model ensemble and
 299 a large ensemble of CanESM5 suggests that internal variability can largely contribute to the total
 300 uncertainty in the extreme precipitation rates, when estimated from one single simulation, even

301 in a very high emission scenario. Figure 3 illustrates this influence of internal variability on the
 302 total uncertainty. The figure depicts the ratio of the width of the confidence range (the difference
 303 between 90% and 10% quantiles) of the CanESM5 large ensemble to that of the CMIP6 cross
 304 model ensemble. We see that for mean extreme precipitation rates scaled by global mean surface
 305 temperature, the internal variability alone could induce a range of response about half as large
 306 as the multi-model spread (global average of $\approx 55\%$). For the high and mid-latitudes regions, the
 307 internal variability is even larger and explains a range of response $\approx 75\%$ (darker shades of blue) as
 308 large as the total uncertainty. These regions exhibit a low to moderate increase in the percentage
 309 response of the extreme precipitation (as shown in figures 1, 2) which in turn argues the strong
 310 influence that internal variability may have on the extreme signals explaining the high percentage
 311 contributions. However, throughout the equatorial belt and the adjacent tropical areas we see a
 312 rather less but non-negligible contribution from the internal variability. Interestingly, most of these
 313 regions fall along with the average position of the ITCZ, which is characterized by high values of
 314 extreme precipitation changes. Here, model uncertainty is the major contributor to the inter-model
 315 spread, whereas internal variability only contributes to about 0-20% but is rather significant enough.

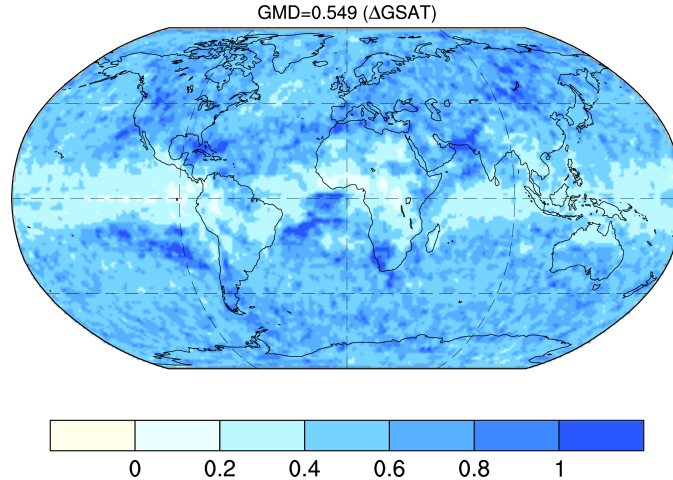


Figure 3: Ratio of the width of confidence range of extreme precipitation in large ensemble CanESM5 to the CMIP6 multi-model ensemble. The result shown here is for scaling with global mean surface temperature change (Δ GSAT).

317 Overall, these results suggest that internal variability contributes substantially to the un-
 318 certainty (i.e., the width of the 80% confidence range) reported in Figure 1. As a consequence,

modeling uncertainty alone is probably narrower than shown in Figure 1. Filtering out internal variability could be done by using several members for each CMIP model involved – but such data are not available so far.

3.4 Sensitivity of precipitation extremes at different global warming levels

Figure 4 provides analyses of the 10%- and 90%- quantiles of global climate sensitivity of RV20 in the CMIP6 ensembles at GWLs of +1.5 K, 2 K, and 3 K respectively. The median changes (figure not shown) relative to the preindustrial period for all GWLs roughly follow a sub-CC rate of $\approx 5\%/K$. Not surprisingly, globally these scaled rates of change in precipitation do not appear to depend on the selected GWL. There is only a slight increase of $0.381\%/K$ in the average multi-model median as the GWL is increased from 1.5K to 3 K possibly due to a non-linear response in some models (e.g., Pendergrass et al. (2019) based on a CMIP5 model), or just a sampling uncertainty. A notable observation as summarized in Table 2 is that the inter-model uncertainty range tends to decrease as the GWL increases. The lower-tail of the extreme precipitation rates shown by 10th percentile maps for the three GWLs (figure 4 left panel) reveals a clear decrease in the average negative precipitation rate values from $-6.403\%/K$ (+1.5K) to $-3.847\%/K$ (+2K) and to $-1.495\%/K$ (+3K). Also as seen from the right panel of Figure 4, the upper-tail of the distribution or the 90th percentile maps show that the upper bound of extreme precipitation rates move closer to the median value from $28.916\%/K$ (+1.5K) to $24.394\%/K$ (2K) and $16.020\%/K$ (3K). This reduced uncertainty for higher GWLs is consistent with the expected contribution of internal variability. At lower GWLs, the forced response remains limited, and the additional noise resulting from internal variability is proportionally larger. This finding provides support for investigating changes in extreme precipitation at high GWLs. Moreover, we notice that the uncertainty at +3K GWL remains larger than that reported in Figure 1. Again, this is consistent with a smaller contribution of internal variability in Figure 1 compared to a +3K GWL – consistent with the fact that SSP5-8.5 leads to global warming higher than +3K in most CMIP6 models, and that estimating changes over a longer period (50-yr in Fig 1, vs 20-yr for GWLs) leads to better filtering of internal variability.

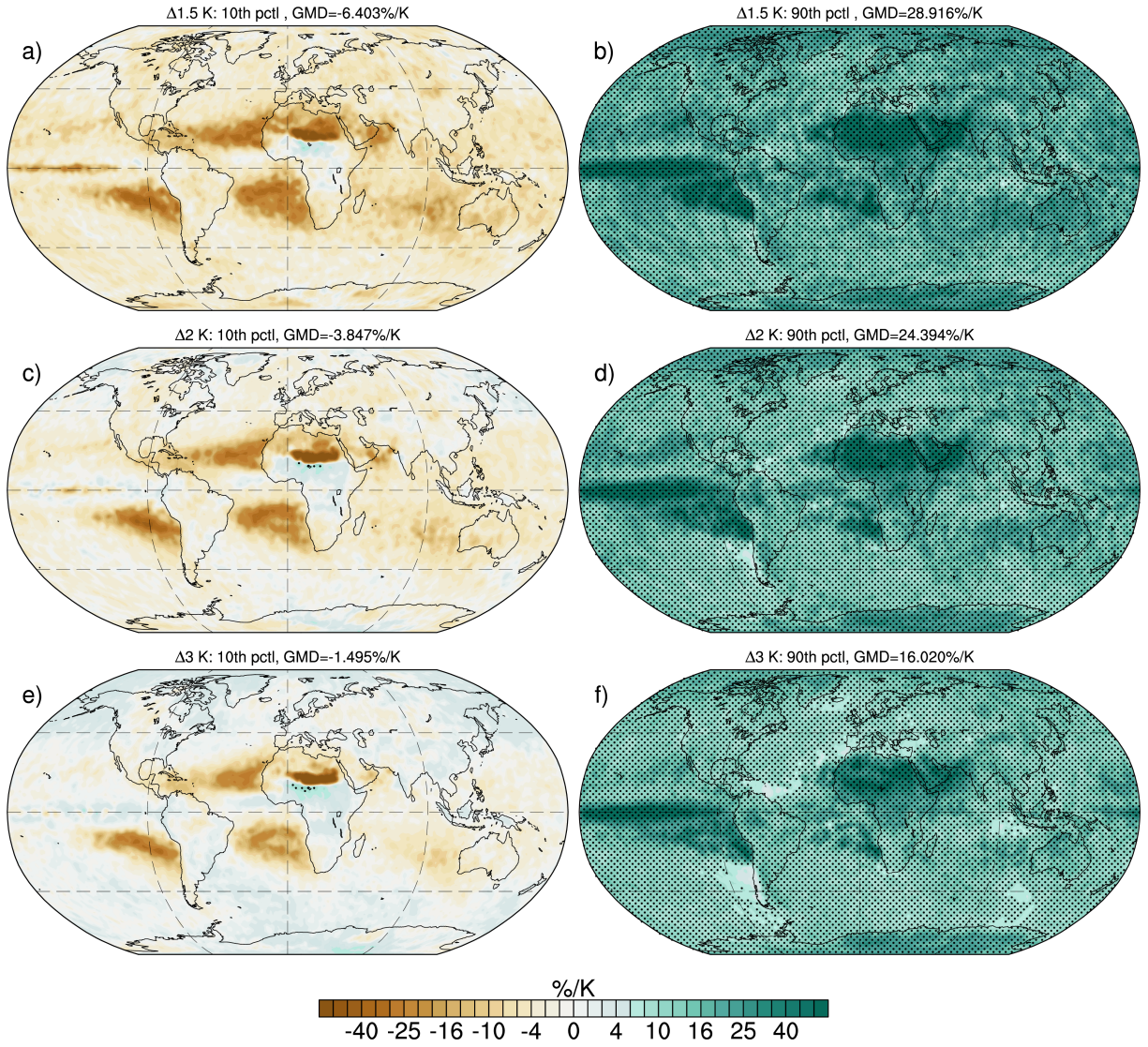


Figure 4: Projected relative changes (%/K) in 20-yr return values of $RX1DAY$ scaled by global mean surface temperature change ($\Delta GSAT$ in $^{\circ}K$) at global warming levels of 1.5, 2 and 3 $^{\circ}K$ above the preindustrial (1850-1900) average values. Left panel shows the 10% quantile maps and right panel shows 90% quantile maps for the CMIP6 multimodel changes. Stippling marks the grid cells where the rate of change is more than 7%/K. GMD denotes the global mean differences.

		10	med	90	width (90-10)
Total	1.5K	-6.403	5.103	28.916	35.319
	2K	-3.847	5.315	24.394	28.241
	3K	-1.495	5.484	16.020	17.515
Land	1.5K	-5.894	5.917	41.466	47.360
	2K	-3.370	6.255	37.421	40.791
	3K	-1.129	6.395	18.163	19.293
Ocean	1.5K	-6.637	4.728	23.193	29.829
	2K	-4.067	4.884	18.456	22.522
	3K	-1.662	5.067	15.039	16.701

Table 2: Areal mean values (in %/K) of 10%- and 90%- quantiles of the extreme precipitation changes scaled by $\Delta GSAT$ over the total global area, global land, and global oceans for three target global warming levels of 1.5, 2, and 3 °K.

3.5 Regions of hypothesis tests

Using a simple hypothesis test as described in Section 2.5, we classified the global areas into three categories. Here we have considered two general hypotheses – (H_0) extreme precipitation does not change with global warming, and (H_1, H_2) the change in extreme precipitation follows the CC rate ($\approx 7\%/K$) for $\Delta GSAT$ and ΔT scaling, respectively. Figure 5 shows the regions categorized accordingly to our hypotheses. Red and blue colors are regions where the hypothesis is rejected while yellow represents regions where the hypothesis is accepted. The top panel in Figure 5 a shows the regions all over the globe where the rate of precipitation change to $\Delta GSAT$ is consistent

354 with $\approx 0\%/K$ (i.e., no change). We see that H_0 is only accepted over limited regions in the globe
 355 where the median values of the projected precipitation changes are consistently low. The same
 356 results are found for the local temperature scaling (with a correlation $\approx 99\%$). Over these regions,
 357 the cohort of CMIP6 models does not provide robust evidence that global warming will intensify
 358 extreme precipitation. A notable feature here is the similarity of the figure 5a to the patterns of
 359 negative dynamic contribution as observed in figure 3 of Pfahl et al. (2017) for the CMIP5 models.
 360 This implies a consistency between the CMIP5 and CMIP6 projections of extreme precipitation,
 361 possibly for a common reason, perhaps, a less robust dynamical response. The negative dynamic
 362 factors may perchance responsible for keeping the extreme precipitation not to increase at large
 363 as it does with moisture increase in the rest of the globe. Remarkably, there is no region where
 364 extreme precipitation is robustly expected to decrease in response to global warming.

365 Figure 5 b, c shows the regions where the hypotheses H_1 , H_2 are accepted or rejected.
 366 Both H_1 and H_2 are used for identifying the regions where the extreme precipitation changes are
 367 consistent with the CC rate of $\approx 7\%/K$ with respect to $\Delta GSAT$ and ΔT respectively. These maps
 368 can be used as a blueprint to identify the regions which are consistent with the CC rate and those
 369 which are not. The first outcome is that a vast majority of places on Earth (about 94% of the
 370 global land area) are expected to undergo a change in extreme precipitation that is consistent with
 371 the CC rate, particularly with the $\Delta GSAT$ scaling. Only a few regions like the Chilean Coast,
 372 South Africa, and part of the Tropical Atlantic Ocean and the Mediterranean exhibit a consistent
 373 sub-CC rate for both temperature scalings. There are also patches of consistent super-CC rates
 374 over the equatorial Pacific and the Sahel region. Scaling with two different temperatures makes
 375 little difference except over the high Northern latitudes. In the Arctic and neighboring land masses,
 376 the expected increase in extreme precipitation does not follow the local warming at the CC rate
 377 (significantly sub-CC). This result is consistent with the enhanced warming expected over these
 378 regions, while the surrounding oceans (the main source of moisture) are warming less quickly.

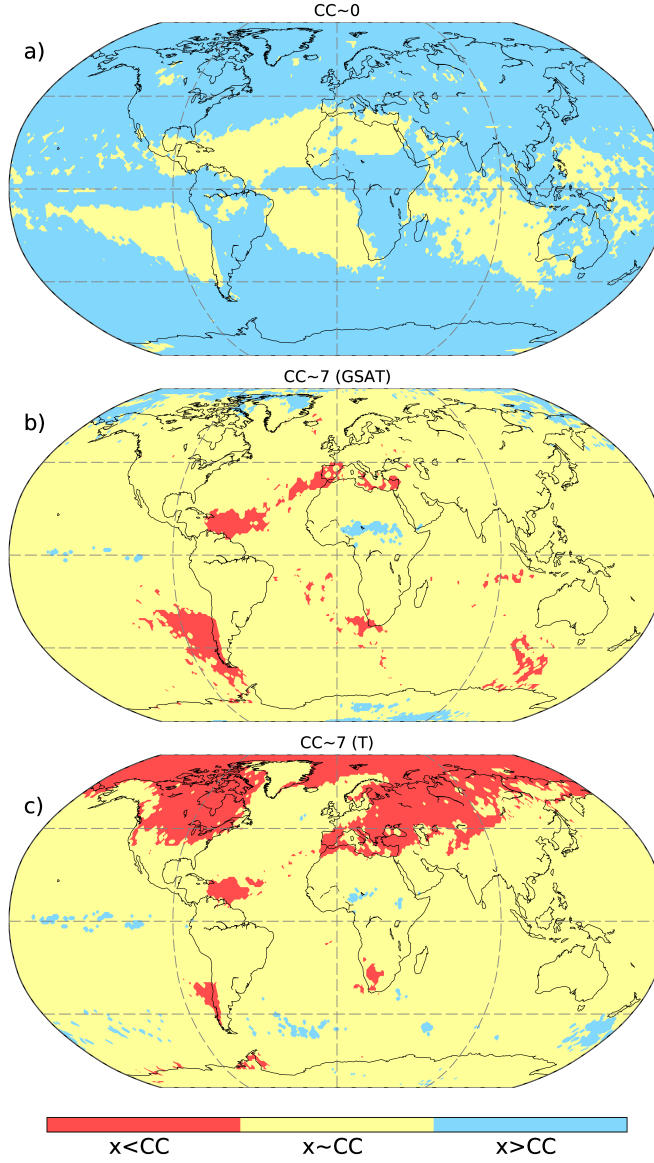


Figure 5: Global maps of confidence areas (80% confidence interval) for the CMIP6 using 34 individual models with a single realization. The maps show where the rate of extreme precipitation changes is consistent with constant rates of $\approx 0\%/K$ or $\approx 7\%/K$. Red color denotes the regions where the changes are always less than the constant, yellow denotes areas where the constant falls within the confidence interval and blue denotes areas where the rates are always greater than the constant. Map (a) shows the areas where the rate of changes in extreme precipitation remains unchanged or consistent to $0\%/K$ when scaled with $\Delta GSAT$. Maps (b), (c) show the global areas where the rate of changes are consistent with the CC rate of $\approx 7\%/K$ with respect to $\Delta GSAT$ and ΔT .

4 Discussions and Conclusions

Despite an overall agreement that extreme precipitation will follow a $\approx 7\%/K$ rate of increase at the global scale, projected changes in extreme precipitation are influenced by multiple factors that can lead to large uncertainties at the regional scale. In this study, we quantify uncertainty in

the projected changes in extreme precipitation – while most studies look at the mean or median change across an ensemble of models – using a single high-emission scenario. We provide a first assessment of the 10-90% range in extreme precipitation responses at the grid-point scale and a global picture of the regions over which changes in extreme precipitation are consistent with the CC rate. Our results suggest that uncertainty is usually quite large. Averaged globally, GSAT scaling ranges extend from about 0 up to about 2 times the CC rate, with a median close to the CC rate. Uncertainty is larger if changes in extreme precipitation are investigated for a given GWL. This may be an artifact of internal variability due to lack of sampling which has a stronger relative contribution at lower levels of warming.

Uncertainty in our ranges comes from both model uncertainty and internal variability, as our calculations are based on one single run from each CMIP6 model. Internal variability can be seen as a basic sampling uncertainty, which could be overcome by averaging across multiple members for each global climate model. Model uncertainty alone would lead to ranges narrower than those reported in this study. However, despite the widening induced by a non-negligible residual contribution of internal variability, our results show that the intensification of extreme precipitation is robust over most regions, with more than 90% of models simulating an increase of 20-yr RVs. This is an important and original result from our study, which increases confidence in the well-known intensification of extreme precipitation. Note that we assume the precipitation extremes remain approximately stationary for our period of analysis, while the use of non-stationary GEV techniques would give similar results.

Most regions around the world exhibit a change consistent with the CC rate of $\approx 7\%/K$. Remarkably about 94% of the global land fraction is characterized by this rate of change when scaled by $\Delta GSAT$. A few exceptions to this include some limited areas over subtropical oceans (showing a significantly sub-CC rate), and parts of the equatorial Pacific and Sahel (showing a significantly super-CC rate). These findings are consistent with well-known changes in large-scale atmospheric circulation, i.e., strengthened subsidence over sub-CC areas, and enhanced convection over super-CC areas. The rate of change in the Arctic is not surprisingly particularly sensitive to the scaling applied, since this region is warming much faster than the global average. This example

411 suggests that the spatial distribution of the warming (e.g., Arctic amplification, land-sea contrast)
412 can be also responsible for departures from the CC rate of intensification.

413 Due to the uncertainty, the rate of change in extreme precipitation depicted here only rep-
414 resents a plausible scenario. This hints at the fact that we cannot produce an accurate projection
415 until we limit the uncertainty. Various types of effort could be undertaken to narrow the uncer-
416 tainty ranges shown in our study. Better filtering of the internal variability would require using
417 ensemble members for each CMIP model – something that is not available at the moment except for
418 a few models. We, therefore, suggest to the modeling community to consider producing a minimum
419 number of realizations in the forthcoming CMIP7 exercise. Beyond internal variability, evidence
420 suggests that modeling uncertainty also contributes to a large fraction of the reported uncertainty.
421 This source of uncertainty is related to our limited knowledge of the key physical processes con-
422 trolling the response of extreme precipitation that is simulated by both global and regional climate
423 models. Thus the generation of large ensembles along with other improvements like the development
424 and wider use of convection-permitting models (Lucas-Picher et al., 2021) could increase the relia-
425 bility of projected changes in extreme precipitation. Other methods such as the development and
426 application of observational constraints (Ribes et al., 2021) could be also very useful to constrain
427 the response of both global and regional climate models.

428 **Declaration of competing interest**

429 The authors declare that they have no known competing financial interests or personal
430 relationships that could have appeared to influence the work reported in this paper.

431 **Acknowledgements**

432 This work is part of the Climate Advanced Forecasting of sub-seasonal Extremes (CAFE)
433 project, which has received funding from the European Union’s Horizon 2020 research and inno-
434 vation program under the Marie Marie Skłodowska-Curie grant agreement No 813844. We ac-
435 knowledge the World Climate Research Programme’s Working Group on Coupled Modelling, which
436 is responsible for CMIP, and we thank the climate modeling groups for producing and making

437 available their model output to CMIP. We also thank the Institut Pierre-Simon Laplace (ISPL)
438 Mésocentre for Climate Sciences for the CMIP6 data acquisition, storage space, and intensive com-
439 puting resources for this paper.

440 References

441 L. V. Alexander, X. Zhang, T. C. Peterson, J. Caesar, B. Gleason, A. Klein Tank, M. Haylock,
442 D. Collins, B. Trewin, F. Rahimzadeh, et al. Global observed changes in daily climate extremes
443 of temperature and precipitation. *Journal of Geophysical Research: Atmospheres*, 111(D5), 2006.

444 R. P. Allan and B. J. Soden. Atmospheric warming and the amplification of precipitation extremes.
445 *Science*, 321(5895):1481–1484, 2008.

446 M. R. Allen and W. J. Ingram. Constraints on future changes in climate and the hydrologic cycle.
447 *Nature*, 419(6903):228–232, 2002.

448 B. Asadieh and N. Y. Krakauer. Global trends in extreme precipitation: climate models versus
449 observations. *Hydrology and Earth System Sciences*, 19(2):877–891, 2015.

450 M. Bador, M. G. Donat, O. Geoffroy, and L. V. Alexander. Assessing the robustness of future
451 extreme precipitation intensification in the cmip5 ensemble. *Journal of Climate*, 31(16):6505–
452 6525, 2018.

453 P. Berg, J. Haerter, P. Thejll, C. Piani, S. Hagemann, and J. Christensen. Seasonal characteristics
454 of the relationship between daily precipitation intensity and surface temperature. *Journal of*
455 *Geophysical Research: Atmospheres*, 114(D18), 2009.

456 S. C. Chan, E. J. Kendon, S. Berthou, G. Fosser, E. Lewis, and H. J. Fowler. Europe-wide precipi-
457 tation projections at convection permitting scale with the unified model. *Climate Dynamics*, 55
458 (3):409–428, 2020.

459 J. Cohen, J. Screen, J. Furtado, M. Barlow, D. Whittleston, D. Coumou, J. Francis, K. Dethloff,
460 D. Entekhabi, J. Overland, et al. Recent arctic amplification and extreme mid-latitude weather,
461 nat. geosci., 7, 627–637, 2014.

462 H. Douville and A. John. Fast adjustment versus slow sst-mediated response of daily precipitation
463 statistics to abrupt 4xco 2. *Climate Dynamics*, 56(3):1083–1104, 2021.

464 V. Eyring, S. Bony, G. A. Meehl, C. A. Senior, B. Stevens, R. J. Stouffer, and K. E. Taylor.
465 Overview of the coupled model intercomparison project phase 6 (cmip6) experimental design and
466 organization. *Geoscientific Model Development*, 9(5):1937–1958, 2016.

467 R. Hardwick Jones, S. Westra, and A. Sharma. Observed relationships between extreme sub-daily
468 precipitation, surface temperature, and relative humidity. *Geophysical Research Letters*, 37(22),
469 2010.

470 S.-C. Kao and A. R. Ganguly. Intensity, duration, and frequency of precipitation extremes under
471 21st-century warming scenarios. *Journal of Geophysical Research: Atmospheres*, 116(D16), 2011.

472 T. R. Karl and D. R. Easterling. Climate extremes: Selected review and future research directions.
473 *Climatic change*, 42(1):309–325, 1999.

474 T. R. Karl, N. Nicholls, and A. Ghazi. Clivar/gcos/wmo workshop on indices and indicators for
475 climate extremes workshop summary. In *Weather and climate extremes*, pages 3–7. Springer,
476 1999.

477 V. V. Kharin, F. W. Zwiers, X. Zhang, and G. C. Hegerl. Changes in temperature and precipitation
478 extremes in the ipcc ensemble of global coupled model simulations. *Journal of Climate*, 20(8):
479 1419–1444, 2007.

480 V. V. Kharin, F. Zwiers, X. Zhang, and M. Wehner. Changes in temperature and precipitation
481 extremes in the cmip5 ensemble. *Climatic change*, 119(2):345–357, 2013.

482 R. Knutti and D. Masson. D. & a. gettelman (2013). *Climate Model Genealogy: Generation CMIP5*
483 *and How we got there*, pages 1194–1199, 2013.

484 J. Lee, J. Marotzke, G. Bala, L. Cao, S. Corti, J. Dunne, F. Engelbrecht, E. Fischer, J. Fyfe,
485 C. Jones, et al. Future global climate: scenariobased projections and near-term information.
486 *Climate change*, 2021.

487 F. Lehner, C. Deser, N. Maher, J. Marotzke, E. M. Fischer, L. Brunner, R. Knutti, and E. Hawkins.
488 Partitioning climate projection uncertainty with multiple large ensembles and cmip5/6. *Earth*
489 *System Dynamics*, 11(2):491–508, 2020.

490 C. Li, F. Zwiers, X. Zhang, G. Li, Y. Sun, and M. Wehner. Changes in annual extremes of daily
491 temperature and precipitation in cmip6 models. *Journal of Climate*, pages 1–61, 2020.

492 P. Lucas-Picher, D. Argüeso, E. Brisson, Y. Trambly, P. Berg, A. Lemonsu, S. Kotlarski, and
493 C. Caillaud. Convection-permitting modeling with regional climate models: Latest developments
494 and next steps. *Wiley Interdisciplinary Reviews: Climate Change*, page e731, 2021.

495 S.-K. Min, X. Zhang, F. W. Zwiers, and G. C. Hegerl. Human contribution to more-intense precip-
496 itation extremes. *Nature*, 470(7334):378–381, 2011.

497 R. Mizuta and H. Endo. Projected changes in extreme precipitation in a 60-km agcm large ensemble
498 and their dependence on return periods. *Geophysical Research Letters*, 47(13):e2019GL086855,
499 2020.

500 C. J. Muller, P. A. O’Gorman, and L. E. Back. Intensification of precipitation extremes with
501 warming in a cloud-resolving model. *Journal of Climate*, 24(11):2784–2800, 2011.

502 R. Nath, Y. Luo, W. Chen, and X. Cui. On the contribution of internal variability and external
503 forcing factors to the cooling trend over the humid subtropical indo-gangetic plain in india.
504 *Scientific reports*, 8(1):1–11, 2018.

505 B. C. O’Neill, C. Tebaldi, D. P. v. Vuuren, V. Eyring, P. Friedlingstein, G. Hurtt, R. Knutti,
506 E. Kriegler, J.-F. Lamarque, J. Lowe, et al. The scenario model intercomparison project (scenar-
507 iomip) for cmip6. *Geoscientific Model Development*, 9(9):3461–3482, 2016.

508 P. A. O’Gorman. Precipitation extremes under climate change. *Current climate change reports*, 1
509 (2):49–59, 2015.

510 P. Pall, M. Allen, and D. A. Stone. Testing the clausius–clapeyron constraint on changes in extreme
511 precipitation under co 2 warming. *Climate Dynamics*, 28(4):351–363, 2007.

512 A. Pendergrass, D. Coleman, C. Deser, F. Lehner, N. Rosenbloom, and I. Simpson. Nonlinear
513 response of extreme precipitation to warming in cesm1. *Geophysical research letters*, 46(17-18):
514 10551–10560, 2019.

515 A. G. Pendergrass. The global-mean precipitation response to co2-induced warming in cmip6 mod-
516 els. *Geophysical Research Letters*, 47(17):e2020GL089964, 2020.

517 T. Peterson, C. Folland, G. Gruza, W. Hogg, A. Mokssit, and N. Plummer. *Report on the activities*
518 *of the working group on climate change detection and related rapporteurs*. Citeseer, 2001.

519 S. Pfahl, P. A. O’Gorman, and E. M. Fischer. Understanding the regional pattern of projected
520 future changes in extreme precipitation. *Nature Climate Change*, 7(6):423–427, 2017.

521 A. Ribes, S. Qasmi, and N. P. Gillett. Making climate projections conditional on historical obser-
522 vations. *Science Advances*, 7(4):eabc0671, 2021.

523 S. C. Scherrer, E. M. Fischer, R. Posselt, M. A. Liniger, M. Croci-Maspoli, and R. Knutti. Emerging
524 trends in heavy precipitation and hot temperature extremes in switzerland. *Journal of Geophysical*
525 *Research: Atmospheres*, 121(6):2626–2637, 2016.

526 K. Schroeer and G. Kirchengast. Sensitivity of extreme precipitation to temperature: the variability
527 of scaling factors from a regional to local perspective. *Climate Dynamics*, 50(11):3981–3994, 2018.

528 S. Seneviratne, X. Zhang, M. Adnan, W. Badi, C. Dereczynski, A. Di Luca, S. Ghosh, I. Iskandar,
529 J. Kossin, S. Lewis, F. Otto, I. Pinto, M. Satoh, S. M. Vicente-Serrano, M. Wehner, and B. Zhou.
530 Weather and climate extreme events in a changing climate. In Masson-Delmotte, V., P. Zhai,
531 A. Pirani, S. L. Connors, C. Péan, S. Berger, N. Caud, Y. Chen, L. Goldfarb, M. I. Gomis,
532 M. Huang, K. Leitzell, E. Lonnoy, J. B. R. Matthews, T. K. Maycock, T. Waterfield, O. Yelekçi,
533 R. Yu, and B. Zhou, editors, *Climate Change 2021: The Physical Science Basis. Contribution*
534 *of Working Group I to the Sixth Assessment Report of the Intergovernmental Panel on Climate*
535 *Change*, chapter 11. Cambridge University Press, 2021.

536 S. I. Seneviratne. Historical drought trends revisited. *Nature*, 491(7424):338–339, 2012.

537 S. Sherwood, R. Roca, T. Weckwerth, and N. Andronova. Tropospheric water vapor, convection,
538 and climate. *Reviews of Geophysics*, 48(2), 2010.

539 J. Sillmann, V. Kharin, X. Zhang, F. Zwiers, and D. Bronaugh. Climate extremes indices in
540 the cmip5 multimodel ensemble: Part 1. model evaluation in the present climate. *Journal of*
541 *Geophysical Research: Atmospheres*, 118(4):1716–1733, 2013a.

542 J. Sillmann, V. V. Kharin, F. Zwiers, X. Zhang, and D. Bronaugh. Climate extremes indices in the
543 cmip5 multimodel ensemble: Part 2. future climate projections. *Journal of Geophysical Research:*
544 *Atmospheres*, 118(6):2473–2493, 2013b.

545 M. Sugiyama, H. Shiogama, and S. Emori. Precipitation extreme changes exceeding moisture
546 content increases in miroc and ipcc climate models. *Proceedings of the National Academy of*
547 *Sciences*, 107(2):571–575, 2010.

548 Q. Sun, X. Zhang, F. Zwiers, S. Westra, and L. V. Alexander. A global, continental, and regional
549 analysis of changes in extreme precipitation. *Journal of Climate*, 34(1):243–258, 2021.

550 N. C. Swart, J. N. Cole, V. V. Kharin, M. Lazare, J. F. Scinocca, N. P. Gillett, J. Anstey, V. Arora,
551 J. R. Christian, S. Hanna, et al. The canadian earth system model version 5 (canesm5. 0.3).
552 *Geoscientific Model Development*, 12(11):4823–4873, 2019.

553 C. Tebaldi, K. Hayhoe, J. M. Arblaster, and G. A. Meehl. Going to the extremes. *Climatic change*,
554 79(3):185–211, 2006.

555 K. E. Trenberth. Changes in precipitation with climate change. *Climate Research*, 47(1-2):123–138,
556 2011.

557 N. Utsumi, S. Seto, S. Kanae, E. E. Maeda, and T. Oki. Does higher surface temperature intensify
558 extreme precipitation? *Geophysical research letters*, 38(16), 2011.

559 J. Vial, J.-L. Dufresne, and S. Bony. On the interpretation of inter-model spread in cmip5 climate
560 sensitivity estimates. *Climate Dynamics*, 41(11-12):3339–3362, 2013.

561 G. Wang, D. Wang, K. E. Trenberth, A. Erfanian, M. Yu, M. G. Bosilovich, and D. T. Parr.
562 The peak structure and future changes of the relationships between extreme precipitation and
563 temperature. *Nature Climate Change*, 7(4):268–274, 2017.

564 M. Wehner, P. Gleckler, and J. Lee. Characterization of long period return values of extreme daily
565 temperature and precipitation in the cmip6 models: Part 1, model evaluation. *Weather and*
566 *Climate Extremes*, 30:100283, 2020.

567 M. F. Wehner. Characterization of long period return values of extreme daily temperature and
568 precipitation in the cmip6 models: Part 2, projections of future change. *Weather and Climate*
569 *Extremes*, 30:100284, 2020.

570 S. Westra, L. V. Alexander, and F. W. Zwiers. Global increasing trends in annual maximum daily
571 precipitation. *Journal of climate*, 26(11):3904–3918, 2013.

572 K. Wyser, T. v. Noije, S. Yang, J. v. Hardenberg, D. O’Donnell, and R. Döscher. On the increased
573 climate sensitivity in the ec-earth model from cmip5 to cmip6. *Geoscientific Model Development*,
574 13(8):3465–3474, 2020.

575 M. D. Zelinka, T. A. Myers, D. T. McCoy, S. Po-Chedley, P. M. Caldwell, P. Ceppi, S. A. Klein,
576 and K. E. Taylor. Causes of higher climate sensitivity in cmip6 models. *Geophysical Research*
577 *Letters*, 47(1):e2019GL085782, 2020.

578 W. Zhang, G. Villarini, and M. Wehner. Contrasting the responses of extreme precipitation to
579 changes in surface air and dew point temperatures. *Climatic change*, 154(1):257–271, 2019.